ADVANCED ELECTRONIC MATERIALS
www.advelectronicmat.de

Check for updates

Vertical Heterostructures between Transition-Metal Dichalcogenides—A Theoretical Analysis of the NbS2/WSe2 Junction

Zahra Golsanamlou, Poonam Kumari, Luca Sementa, Teresa Cusati, Giuseppe Iannaccone, and Alessandro Fortunelli**

Low-dimensional metal-semiconductor vertical heterostructures (VH) are promising candidates in the search of electronic devices at the extreme limits of miniaturization. Within this line of research, here a theoretical/computational study of the NbS_2/WSe_2 metal-semiconductor vertical hetero-junction using density functional theory (DFT) and conductance simulations is presented. First atomistic models of the NbS_2/WSe_2 VH considering all the five possible stacking orientations at the interface are constructed, and DFT and quantum-mechanical (QM) scattering simulations are conducted to obtain information on band structure and transmission coefficients. Then an analysis of the QM results in terms of electrostatic potential, fragment decomposition, and band alignment is carried out. The behavior of transmission expected from this analysis is in excellent agreement with, and thus fully rationalizes, the DFT results, and the peculiar double-peak profile of transmission. Finally, maximally localized Wannier functions, projected density of states, and a simple analytic formula to predict and explain quantitatively the differences in transport in the case of epitaxial misorientation are used. Within the class of Transition-Metal Dichalcogenide systems, the NbS_2/WSe_2 VH exhibits a wide interval of finite transmission and a double-peak profile, features that can be exploited in applications.

1. Introduction

2D transition metal dichacogenides (TMDs) have attracted extensive attention in recent years due to their promising applications in electronic and optoelectronic devices.[1–5] In particular, their lateral heterostructures (LHs) and vertical heterostructures (VHs) may allow realizing metal/semiconductor junctions at the ultimate thickness limit, that could be competitive, at the fundamental level of control of the electrostatic potential in the device, with present silicon-based integrated circuit technology.[3,4,6] Device engineering has been shown to play an important role in improving performance of these systems, since issues associated with lattice mismatch and Fermi level pinning in metal-semiconductor devices, and (as we will see later) the presence of a pseudogap below the Fermi level for these nonideal metals can notably affect charge transport.[3,7–9] Experiments have indicated that interfaces based on van der Waals (vdW) forces as in VH instead of covalent ones as in LH can help decrease some of these issues. In VH the heterojunction is realized by stacking one (few) layers of one TMD on top of one (few) layers of a different TMD, and the junction is held together by vdW forces, whereas in LHs the stoichiometry changes from one TMD to another within the same single layer, and the two TMD pieces are held together by covalent/ionic forces. The presence of weaker (dispersion) forces in VH junctions arguably leads to a decrease of the gradient of the electrostatic potential at the interface, as well as reducing the probability of chemical disorder and defect-induced gap states which often occur in LHs (in addition to band engineering effects as we will see later), therefore explaining the typically superior performance of VH-based devices. As a result, vertically stacked heterostructures are a subject of considerable attention for 2D TMD devices.[3,8,10,11]

At the experimental level, Shin et al. investigated charge transport in NbS_2/n(electron acceptor)-MoS_2 VH.[11] They calculated the work function (WF) of NbS_2 and n-MoS_2 and measured the associated Schottky barrier, showing that this barrier affects charge transfer and causes carrier depletion in MoS_2 underneath NbS_2. Also, they showed that the vdW interface between NbS_2 and MoS_2 favors in-plane carrier transport, and that charge transport can be tuned by applying bias and gate voltage. p-n (electron donor–electron acceptor, respectively) VHs composed of two semiconductor TMDs have also been widely studied at both experimental and theoretical level.[12–17]

Z. Golsanamlou, P. Kumari, L. Sementa, A. Fortunelli
CNR-ICCOM and IPCF
Consiglio Nazionale delle Ricerche
via G. Moruzzi 1, Pisa 56124, Italy
E-mail: luca.sementa@cnr.it; alessandro.fortunelli@cnr.it
T. Cusati, G. Iannaccone
Dipartimento di Ingegneria dell'Informazione
Università di Pisa
Via G. Caruso 16, Pisa 56122, Italy

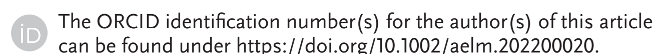
The ORCID identification number(s) for the author(s) of this article can be found under https://doi.org/10.1002/aelm.202200020.

© 2022 The Authors. Advanced Electronic Materials published by Wiley-VCH GmbH. This is an open access article under the terms of the Creative Commons Attribution-NonCommercial-NoDerivs License, which permits use and distribution in any medium, provided the original work is properly cited, the use is non-commercial and no modifications or adaptations are made.

DOI: 10.1002/aelm.202200020

 © 2022 The Authors. Advanced Electronic Materials published by Wiley-VCH GmbH

Huo et al. studied the transport properties of the WS_2/MoS_2 VH[15] via band structure calculations, showing that the bottom of the conduction band (BCB) and the top of the valence band (TVB) of WS_2 are higher in energy than those of MoS_2, so that electrons are transferred from WS_2 into MoS_2. Lee et al. investigated the optoelectronic properties of the WSe_2/MoS_2 VH.[16] They reported that charge transport occurs mostly in the vertical direction due to the voltage drop at the interface of the p–n junction, without a significant potential barrier. Therefore, charge transfer occurs via interlayer tunneling of majority carriers between the BCB of MoS_2 and the TVB of WSe_2. Band alignment of $MoS_2/MoTe_2$ vdW heterojunction on a SiO_2 substrate was calculated by Lim et al. using data extracted from scanning Kelvin probe microscopy.[17] The work functions of the individual $MoTe_2$ and MoS_2 phases turned out to be identical, implying that MoS_2 has a slightly higher work function in the heterojunction. This change in work function was assumed to be due to charge transfer between the two TMDs and also to trap charges in the SiO_2 substrate. They also used gate voltage and bias to change the type and rate of charge transfer. Without a gate bias, they showed that the junction between the MoS_2 n-channel and the $MoTe_2$ p-channel has almost no barrier, but there is a built-in potential for the MoS_2 n-channel due to the difference in work functions. Transport properties of vertical semiconductor/metal and metal/metal heterojunctions made of TMDs (MoS_2/NbS_2, $MoSe_2/NbS_2$, $NbS_2/NbSe_2$, and $CoS_2/CoSe_2$) along with their electronic properties were studied by Costa et al.[18] They confirmed that, because of the large work function of the metals (NbS_2 and CoS_2), the TVB of the semiconductor is typically positioned above the Fermi energy of the metal. They also discussed how the alignment of the projected density of states (PDOS) in the metal and semiconductor phases and the pinning of the TVB of the latter to the Fermi level of the former makes that the junction show a diode-like behavior.

We underline that the phenomenon by which the TVB of the semiconductor is pinned at the Fermi energy of the metal is of crucial importance in these systems (as we will see hereafter), and in this respect these 2D materials behave almost exactly as their 3D counterparts. In general, the tunneling barrier at the interface of metal-semiconductor junction has thus typically a Schottky character. There are different ways in literature to calculate the Schottky barrier height (SBH). Jelver et al. analyzed the slope of density of states (DOS) and the transmission values to estimate the SBH.[19] They also showed that the presence of localized states due to the interface or to doping can modulate the barrier height. In previous work, we estimated the SBH from the jump in electrostatic potential at the interface,[20] i.e., by the difference between the local Fermi energy of the metallic part and the local TBV of the semiconductor part precisely at the interface, where a fragment-analysis method was used to obtain the needed alignment of the two components.[21] The origin and nature of Schottky barriers in TMD monolayers (MX_2 where M = Mo, W, and X = S, Se, Te) in contact with an ideal metal electrode have been studied by Szczęśniak et al.[22] using combination of the complex band structure formalism and the cell-averaged Green's function technique. They found the charge neutrality level (CNL) and calculated the SBH as the difference between the CNL and the metal work function. They noted that the CNL lie at the midpoint of the semiconducting bandgap, and attributed the origin of SBHs to metal induced gap states (MIGs), analogously to the case of 3D metal-semiconductor junctions. The SBHs of 2D TMD(MoS_2, $MOSe_2$, $MOTe_2$)/metal(Sc, Mg, Al, Ti, Cr, Mo, Ru, Co, Ni, Pd, Pt, MoO_3) junctions for both top and edge contact geometries have also been studied by Guo et al.,[23] showing that for both the edge and top contact geometries, SBHs are pinned to the Fermi energy of the metal with similar pinning factor. This was attributed to the direct bonding between the contact metal atom and TMD chalcogen atom in both cases.

Using density-functional theory (DFT) Ren et al. considered the different stacking of GeC on TMD_2 (MoS_2, $MoSe_2$, WS_2, and WSe_2) and studied electronic structure and electrostatic potential for the most stable vdW geometries.[24] An atom-projected band structure analysis of the heterostructure showed that the TMDs and GeC preserve their direct bandgaps, and the bandgap of each studied heterostructure is less than the bandgap of the constituent systems. The analysis of band alignment indicates electron transfer from TMDs to GeC which causes a potential drop and a built-in electric field across the vdW heterostructure. Cusati et al. investigated the effect of the stacking sequence on vertical electron transport in MoS_2 multilayer systems[25] and concluded that interlayer electron transport is strongly dependent on the stacking of the MoS_2 layers, and that the interlayer distance (related to mis-orientation phenomena) also affects the transmission coefficient. Work function engineering for metal/semiconductor VHs was investigated by Ding et al.[26,27] They considered 2D H(phase)- and T(phase)-MX_2 (M = Ti, V, Nb, Ta, Mo, and W; X = S and Se) as metals and H-WSe_2 as semiconductor, respectively. They extracted the value of the SBH from an analysis of band edge position, investigated the behavior of the SBH as a function of the work function of the different metals, and quantified the strength of pinning in terms of the derivative of the SBH with respect to the metal work function. They found that the ideal Schottky–Mott limit is approached when the SBH changes exactly in parallel with the work function as occurring in the region of low values of the metal work function, whereas a strong pinning-like behavior is found to occur in the Ohmic contact region of high values of the metal work function. Hu et al. studied the electronic structure, band alignment, and potential barrier for the 1T(phase)VSe_2/multilayer-MoSSe VH, together with other Schottky systems for comparison, including WSe_2,[8] in the search for Ohmic contacts. They found that Schottky and tunnel barriers of 1T(phase)VSe_2/multilayer-MoSSe VH can be regulated by changing the vdW stacking at the interface, or by applying a tensile strain: by decreasing the BCB and increasing the TVB of VSe_2, the Schottky-to-Ohmic contact transition can be achieved.

Here, we study the NbS_2/WSe_2 2H-bulk VH as a prototype of metal-semiconductor VH hybrid interface. After building realistic structural models, we consider the 5 possible orientations of the layers at the interface (5 different stackings), derive their band structure, and calculate transmission coeffcients in these systems, finding a nonzero interval wider than in the corresponding LH and an interesting double-peak profile of transmission. We then apply an analysis of electron transport via two tools: 1) fragment decomposition and electrostatic

 © 2022 The Authors. Advanced Electronic Materials published by Wiley-VCH GmbH

potential analyses, and 2) alignment of the PDOS of the atoms in the scattering region. With these tools, we are able to fully rationalize the behavior of the transmission coefficient and its double-peak profile in the case of minimal-distance interlayer epitaxy, tracing back the double peak profile ultimately to the presence of a pseudogap below the Fermi energy in NbS_2, as is typical in the DOS of these nonideal metallic layered materials. However, we find that band structure and alignment analysis is not able to explain transport when the stacking distance at the interface is increased to that expected for mis-oriented (orientationally mis-matched) stackings. We then introduce a simple model combining atomic PDOS and hopping elements at the interface as derived from a Wannier analysis of the wave function, and show that this model can now accurately explain the computational results, in particular the presence or absence of a double-peak profile in transmission depending on interfacial distances. Also, in comparison with the homologous WSe_2/NbS_2 LH,[20] the wide-interval and double-peak-profile transmission here found for the VH system is of interest for potential applications, while the theoretical fragment, alignment, and Wannier analysis of electronic transmission should be generally applicable to the study of transport in 2D materials. Band alignment in VH also depends on the local pressure. A change in pressure will change interlayer distances which in turn will affect the tight-binding hopping matrix elements as well as the DOS, so that one expects significant changes in the SBH as well as in transmission as a function of pressure. Indeed, de Araújo et al. studied the change in Schottky barrier as a function of applied force (pressure),[28] finding that SBH changes at a rate of 0.21 (for a few layers MoS_2), 0.23 (for three layers MoS_2), and 0.78 (for two layers MoS_2) meV nN^{-1}.

The article is organized as follows. The computational approach is presented in Section 2. Section 3 presents and discusses our main results, while conclusions are summarized in Section 4.

2. Computational Methods

Electronic structure calculations were performed using Quantum Espresso (QE) package,[29,30] using 50 Ry as energy cutoff for the wave function and 500 Ry as density cutoff for the density, and large 22×22×1 Monkhorst–Pack *k*-meshes to sample the Brillouin zone. A plane-wave basis set, a gradient-corrected exchange-correlation (xc-)functional [the Perdew–Burke–Ernzerhof (PBE)][31] and scalar-relativistic ultrasoft pseudopotentials were utilized.

Transmission simulations were carried out based on a scattering state approach considering right-ward propagating modes from the left to the right electrode as implemented in the QE/PWcond routine[32,33] in the limit of ballistic transport. In the transmission simulations, the same (22 × 22 × 1) *k*-mesh as in QE/PWscf (see Section S1, Supporting Information) was used. The DFT band structure was then analyzed to derive Hamiltonians based on maximally localized Wannier functions via the Wannier90 code,[34,35] using transition-metal *d*-orbitals and chalcogenide *p*-orbitals in the basis set. More details about Wannier90 are given in the Supporting Information.

Five stacking geometries are possible in a VH between two TMD layered systems,[8,25] conventionally denoted as: AA', AB', AB, AA, A'B, as depicted in **Figure 1**. Using a more illustrative and physically clearer notation, focusing on the atoms of the two monolayers at the interface, AA' can be denoted as ABA/BAB, where A,B,C are the conventional positions in (111) stacking and correspond, in order, to the positions of: (first S atoms in NbS_2)(Nb in NbS_2)(second S atoms in NbS_2)/(first Se atoms in WSe_2)(W in WSe_2) (second Se atoms in WSe_2). Here all the 5 possible stackings were considered between NbS_2 and WSe_2 phases assumed in 2H bulk arrangement, i.e.:

a) AA': the stacking of atoms at the interface can be described as ABA/BAB, thus S/Se first-neighbors are in hollow positions, the S atoms eclipse W atoms, and the Se atoms eclipse Nb atoms—AA' corresponds to the bulk 2H stacking;
b) AB': the stacking at the interface is ABA/BCB, thus S/Se first-neighbors are in hollow positions, and Se atoms eclipse Nb atoms, whereas S atoms are staggered with respect to W atoms—AB' corresponds to the bulk 3R stacking;
c) AB: the stacking at the interface is ABA/CBC, thus S/Se first-neighbors are in hollow positions, while both S-W and Se-Nb are staggered;
d) AA: the stacking at the interface is ABA/ABA, thus S/Se first-neighbors are on top positions, and Nb and W atoms are eclipsed;
e) A'B: the stacking at the interface is ABA/ACA, thus S/Se first-neighbors are on top positions, and Nb and W atoms are staggered.

In short, the major difference among these 5 interfaces is that AA', AB', and AB configurations have first-neighbor S/Se in hollow stacking, i.e., the energetically most stable contact, whereas AA and A'B have first-neighbors S/Se in top stacking: the latter stackings are introduced as models of the energetically less stable contacts induced by misorientation, i.e., a relative rotation, of the NbS_2 and WSe_2 systems in the synthesis process, as discussed[25] and below.

To define the atomic coordinates, experimental input was used from 2H bulk phases, taken from ref. [36] for NbS_2 (a = 3.33 Å, c = 11.95 Å, and S–S intralayer distance = 2.97 Å) and from ref. [37] for WSe_2 (a = 3.282 Å, c = 12.96 Å, and Se–Se intralayer distance = 3.34 Å), respectively. The lattice constant in the direction parallel to the interface was set to a = 3.306 Å, as an average of NbS_2 2H-bulk and WSe_2 2H bulk lattice constants.[36,37] The unit cell describing the NbS_2/WSe_2 VH is constructed by stacking 6 NbS_2 layers, followed by 12 WSe_2 layers and 6 NbS_2 layers, see Figure 1a, with the atomic configuration at the interface arranged according to the 5 stackings defined above. The minimum distance between S and Se atoms at the interface is the same for all the stackings, and is taken as the average of the S–S distance in bulk NbS_2 and Se–Se distances in bulk WSe_2.

Note that the experimental geometries were used for pure phases as input without relaxation in the DFT simulations to avoid artifacts due to a discrepancy between DFT+D3 predicted value and experimental one for the in-plane lattice parameter of NbS_2 (see Table S1 in the Supporting Information). Additionally,

© 2022 The Authors. Advanced Electronic Materials published by Wiley-VCH GmbH

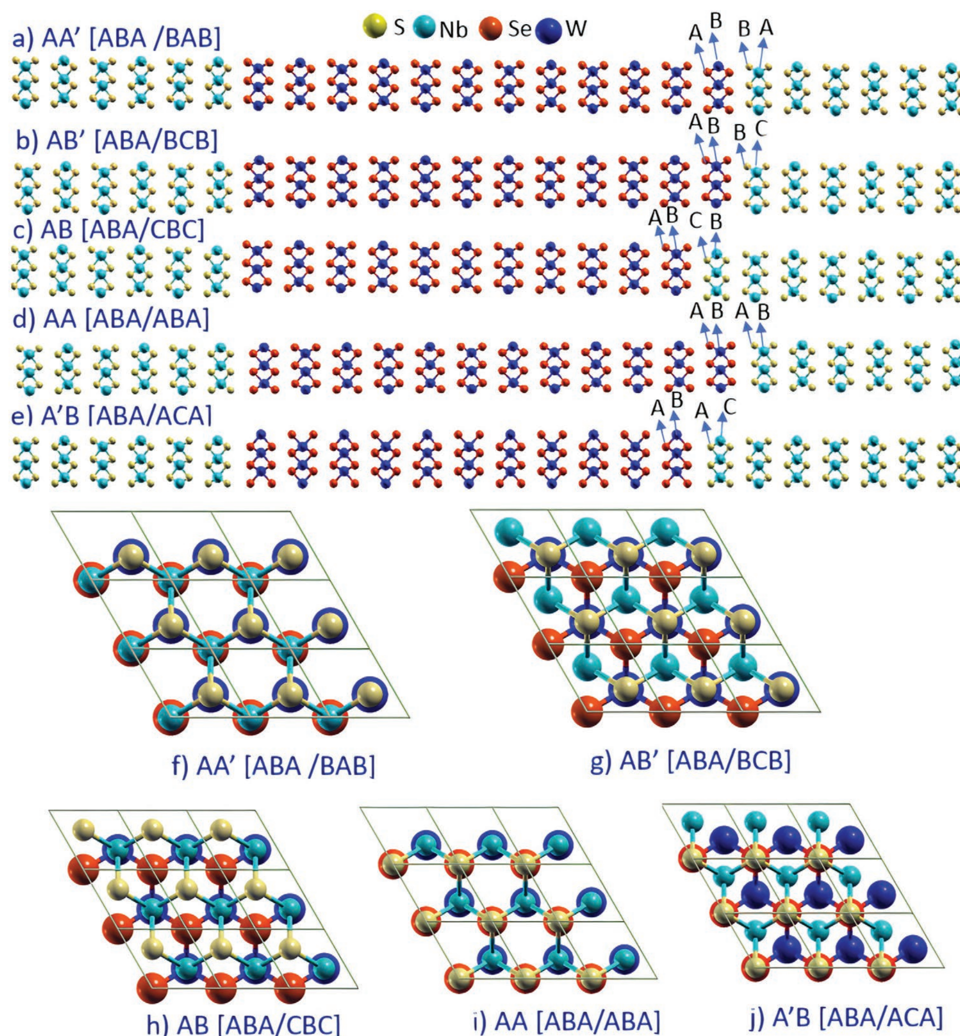

Figure 1. The five stacking geometries considered for the NbS_2/WSe_2 VH, representing Nb atoms are in cyan color, S atoms are in yellow, W atoms are in dark blue and Se atoms are in dark orange. a–e) side views: a) AA'[ABA/BAB] in the left interface TM atom from last NbS_2 layer goes on top of X (chalcogen atom) of the first WSe_2 layer—in the right interface the TM atom of the last WSe_2 layer goes on top of the X atom of the first NbS_2 layer. b) AB'[ABA/BCB] in the left interface the TM atom of last NbS2 layer goes on the top of the X atom of first WSe2 layer, while the X atom from the NbS2 layer goes in the hollow position of the WSe2 layer. c) AB[ABA/CBC] in the left interface the TM atom from the last NbS_2 layer goes on top of the TM atom of the first WSe_2 layer, while the X atoms from the WSe_2 layer sit in the hollow position of the NbS_2 layer. d) AA [ABA/ABA], in the left interface the TM and X atoms from the last NbS_2 layer are stacked over the TM and X atoms of the first WSe_2 layer—in the right interface the TM and X atoms of last WSe_2 layer stacked over TM and X atoms of first NbS_2 layer, and e) A'B [ABA/ACA], in the left interface the X atom from last NbS_2 layer goes on top of X atom from the first WSe_2 layer, while the TM atoms from one layer at the interface sits on the hollow position of the next layer. In the right interface the X atom from last WSe_2 layer goes on top of the X atom from the first NbS2 layer, while the TM atoms of the NbS2 layer sit in a hollow position of WSe_2 layer. f–l) top views of the structures which shows the right interface of the structure explicitly: f) AA', g) AB', h) AB, i) AA, and l) A'B.

in the absence of experimental data, an average value was used for the interlayer distance at the interface: this corresponds to a minimum in the total energy as predicted by the DFT+D3 approach, see Figure S2 in the Supporting Information (where more information is also provided).

understanding its behavior in terms of constituent fragments, using the electrostatic potential as a unifying descriptor. Comparison with a previous study on the LH of the same NbS_2/WSe_2 materials combination[20] will allow us to assess the relative merits of the two interfaces.

3. Results and Discussion

We performed DFT and transport simulations on the configurations built in Section 2, and complemented them with an analysis[21] based on partitioning a composite system and

3.1. Electrostatic Potential Analysis

Focusing on the AA' stacking which corresponds to the lowest-energy (2H-like) interface, we conducted an electrostatic potential analysis[21] as illustrated in **Figure 2**.

 © 2022 The Authors. Advanced Electronic Materials published by Wiley-VCH GmbH

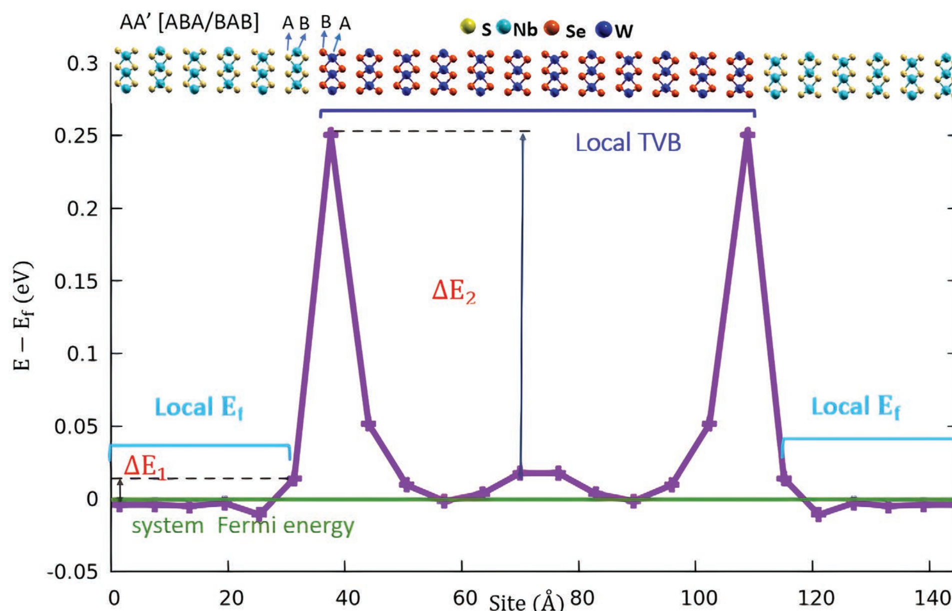

Figure 2. Electrostatic potential profile of NbS2/WSe2 VH stack AA' with configuration ABA/BAB at the interface, ΔE_1 is the difference between the local E_f at the interface and lead (middle of NbS_2 part) where ΔE_2 is the difference between the local TVB at the intertface and middle of WSe_2.

In Figure 2, we plot the electrostatic potential on Nb and W atoms, shifted and aligned using quantities extracted from the corresponding fragment phases (NbS_2 and WSe_2), as discussed[21] and applied to the NbS_2/WSe_2 LH,[20] so that the final plot corresponds to the local Fermi energy (loc-E_F) for the NbS_2 metallic fragment and the local top of the valence band (loc-TVB) for the WSe_2 semiconductor fragment. In practice, we build up a fragment 2H bulk NbS_2 phase by replicating the geometry in the middle of the NbS_2 phase, we extract from this calculation the difference between the Fermi energy (E_F) of the system and the electrostatic potential on the Nb atom, and we report this difference onto the NbS_2/WSe_2 VH by adding it to the values of the electrostatic potential on Nb atoms in the scattering region, thus finally determining the local Fermi energy. Analogously, we build up a fragment 2H-bulk. WSe_2 phase by replicating the geometry in the middle of the WSe_2 phase, we extract the difference between the TVB and the electrostatic potential on the W atom in this WSe_2 fragment, and we finally add this difference to the values of the electrostatic potential on W atoms in the scattering region to obtain the loc-TVB.

Flatness of the loc-E_F profile at the edges and of the loc-TVB in the middle of the unit cell guarantees convergence of the NbS_2 and WSe_2 fragments, i.e., guarantees that they are sufficiently far from (not affected by) the interfaces, and ensures precise projection of the wave function of the scattering system onto the wave function of the reference system in the successive transmission simulations. Incidentally, we observe that the concavity of the loc-TVB profile near the interfaces in Figure 2 indicates that the electronic density is transferred from WSe_2 to NbS_2 (see the discussion in ref. [21]), which is consistent with band-structure alignment considerations. Note that we expect zero electric field inside the NbS_2 metallic phase so that the loc-E_f should be flat, as it is indeed, whereas the profile of the loc-TVB is slightly more complex as a consequence of band bending and charge dipole effects at the metal/semiconductor interface.

The electrostatic potential analysis for the other stackings are reported and discussed in the Supporting Information, Section 3. We note that the jump in the electrostatic potential at the interface in Figure 2 provides an estimate of the Schottky barrier for the NbS2/WSe2 metal/semiconductor VH interface, of the order 0.24 eV for the AA' configuration and changing slightly as a function of stacking (see Figure 2; and Figure S3, Supporting Information). Our method qualitatively correlates with the CNL approach,[22] but the SBH estimate derived from the atomistic analysis comes out to be quantitatively smaller than the canonical estimate because the use of an atomistic NbS_2 TMD metal versus an ideal metal (conductor) decreases the jump in the electrostatic potential at the interface. We finally add that one limitation of our approach is that we assume a rigid shift of the electronic states following the shift in the background potential, so that we expect that, when the electronic wave function at the interface is strongly deformed by large dipole moments, our method may become less accurate.

3.2. Transmission Simulations and Analysis

We performed transmission simulations for the configurations corresponding to all 5 considered stackings, always checking that the systems exhibit a flat potential (zero electric field) far from interfaces in the middle of the NbS_2 and WSe_2 regions, so that these regions can be used as leads in the transmission simulations (see Figure 2; and Figure S3, Supporting Information). Since AA' is the most stable system, we start with a detailed analysis of its transmission first.

3.2.1. The AA' Stacking

Figure 3 reports transmission for the AA' stacking. Figure 3 is qualitatively similar to the analogous curve for the NbS_2/WSe_2

 © 2022 The Authors. Advanced Electronic Materials published by Wiley-VCH GmbH

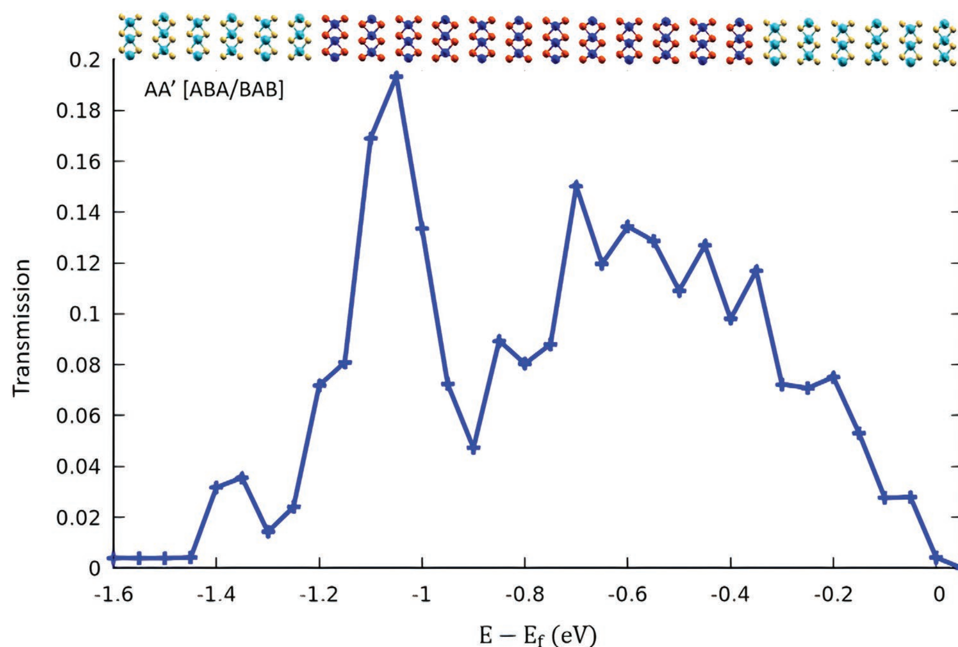

Figure 3. Transmission curve for the NbS2/WSe2 VH with 2H stacking in the Bulk and AA' configuration at the interface.

LH (Figure 3 in ref. [20]), but with two important differences: 1) the range of finite transmission is much more extended (more than 1 eV here vs ≈0.2 eV in the LH), and 2) the curve shows a double peak structure with a minimum around −0.9 eV bias. Both these differences can be useful in applications, although the peaks are not located close to the Fermi level and Fermi level engineering would probably be necessary to use this feature in actual devices. Hereafter we demonstrate how they can be rationalized in simple terms via an electrostatic potential and fragment analysis.

In **Figure 4**, we analyze transmission via two complementary and consistent approaches.

First, we report in Figure 4a,b the band structure and in Figure 4c,d the DOS plots for the NbS_2 and WSe_2 fragment phases, showing that WSe_2 is a semiconductor and NbS_2 is a nonideal metal exhibiting a pseudogap below the Fermi level. It can be noted that the DOS plots in Figure 4c,d exhibit intervals with high values of the DOS, highlighted with strong-green-colored bars, as well as intervals with intermediate to low values, highlighted with light-green-colored bars, and finally intervals with low DOS values, highlighted with yellow-colored bars. If we now draw these bars vertically and align them along the transmission direction by shifting their centers according to the electrostatic potential profile of Figure 2, we get the picture of Figure 4e. In other words, we align the colored bars by positioning them horizontally on the Nb and W atoms in the scattering region, and by shifting them vertically according to the values of the electrostatic potential on the corresponding atoms in the profile of Figure 2. Figure 4e quickly provides a pictorial count of the number of states available for transmission at any given value of the bias, thus allowing us to estimate the regions in which transmission is finite and the overall shape of transmission: a low number of available states corresponds to lower values of the transmission coefficient, while an increase (decrease) in the DOS is expected to bring about a peak (dip) in the transmission coefficient. The consistency of this approximate estimate with the actual transmission results reported for clarity on the left-hand-side of Figure 4e can be immediately appreciated. In more detail, transmission goes to zero above the Fermi energy because the TVB of WSe_2 is pinned at the Fermi energy E_F, and no states are available for electron transport above it (they fall in the bandgap of WSe_2). Moreover, the drastic changes in DOS of the NbS_2 fragment around −0.65 to −1.2 eV are responsible for double peak behavior of transmission coefficient: the dip in transmission around −0.9 eV is understood as being caused by the corresponding dip in the NbS_2 DOS connected with its pseudobandgap.

In Figure 4f, we report PDOS plots, i.e., DOS projected onto individual atoms, that allow for an alternative analysis. As one can see in Figure 2, electrostatic potential jumps are largest for the atoms at the interface. We then focus on these interfacial atoms and contrast them with the atoms in the middle of each component phase (WSe_2 and NbS_2), including PDOS plots projected on both metal and chalcogenide atoms. First, these PDOS plots confirm the counting of states available for transmission from Figure 4e: the larger the PDOS, the larger the transmission around that energy (i.e., a peak in transmission), whereas a small PDOS for some of the atoms corresponds to a dip (valley) in the transmission coefficient. Second, we focus on the shift of the PDOS of Nb and W atoms between the middle of the corresponding fragment and the interface. We have highlighted these shifts as ΔE_1 and ΔE_2 in Figure 4f for Nb and W, respectively, and they read $\Delta E_1 = 0.03$ eV, $\Delta E_2 = 0.284$ eV, thus quantitatively coinciding with the corresponding differences in the atomic electrostatic potentials in Figure 2. The double-peak structure in transmission can thus be explained in terms of these two alternative and consistent analyses of PDOS shape and alignment.

 © 2022 The Authors. Advanced Electronic Materials published by Wiley-VCH GmbH

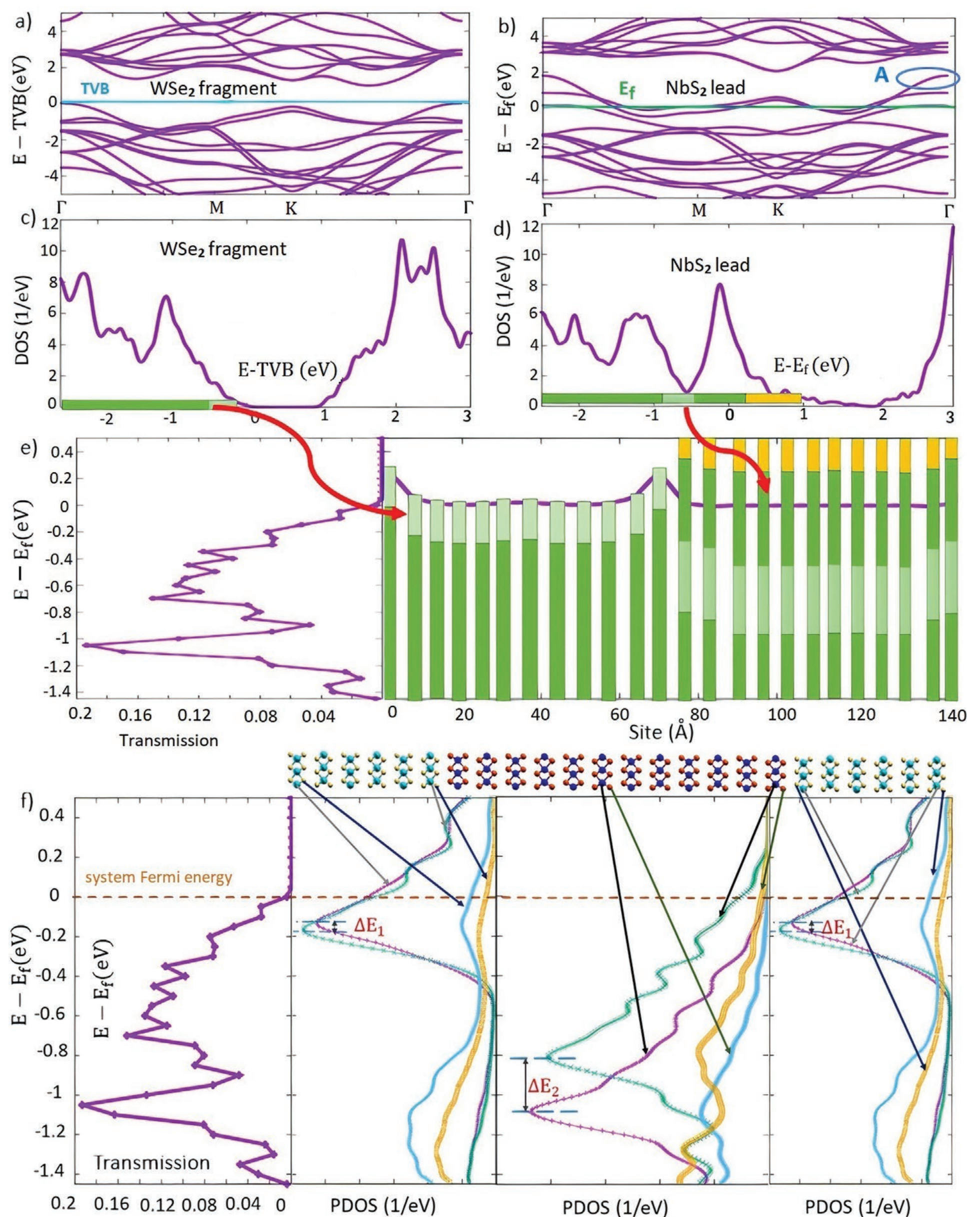

Figure 4. Transmission behavior analysis of NbS2/WSe2 VH (AA') structure: a) band structure of WSe_2 fragment, b) band structure of NbS_2 fragment, A is the TVB of NbS_2. c) DOS of WSe_2 fragment, and d) DOS of NbS_2 fragment (the fragments are taken far from the interfaces in the scattering region), e) transmission of AA' and band alignment procedure to find the states for electron transmission using the obtained color bar from DOS of the fragments in c) and d) in place of loc-E_f and loc-TVB, and f) transmission of AA' and PDOS alignment to find the states for electron transmission. We choose atoms at the interface and far from the interface to do alignment using the PDOS of those atom. Note that ΔE_1 is the shift between the PDOS of atoms from the middle and interface in NbS_2 part and ΔE_2 is the shift between the PDOS of atoms from the middle and interface in part WSe_2.

For comparison, we have also performed transmission simulations for pure NbS_2 (12 layers) and pure WSe_2 (12 layers), and report these results in Figure S4 of the Supporting Information. As one can see from Figure S4 (Supporting Information), the transmission profile of the VH phase can be approximately interpreted as a convolution of the transmission plots of the pure phases, after proper alignment.

In a previous work[20] we have studied electronic transmission in the NbS_2/WSe_2 LH, that we also report in Figure S5 of the Supporting Information for ease of comparison (see Figure 4 of ref. [20]). Two major differences can be appreciated with respect to the present NbS_2/WSe_2 VH: first, a much wider energy interval of nonzero transmission; second, a double-peak structure in the VH case, absent in the LH. These differences can be rationalized. We note in fact that the LH[20] is between monolayer (ML) systems, whereas the present VH involves bulk systems: this leads to distinct differences in the DOS and, in turn, in the transmission. A change in the number of layers from ML to bulk induces a change in the DOS and the band structure of the fragments (see Figure 4; and Figure S5,

 © 2022 The Authors. Advanced Electronic Materials published by Wiley-VCH GmbH

Supporting Information), especially for the NbS_2 component: in the bulk system, at variance with the ML system, the DOS of the NbS_2 fragment does not have a gap below E_F, but rather a dip. A pseudogap is typically present in TMD (nonideal) metallic layered materials below the Fermi energy, and in this respect NbS_2 is a paradigmatic example, but at the monolayer level the pseudogap becomes a real gap. We can thus explain the two major differences of the present results with respect to the NbS_2/WSe_2 LH[20]: the DOS of the NbS_2 fragment does not have a gap below E_F, but rather a dip around –0.7/–0.9 eV with respect to E_F. Correspondingly, the transmission coefficient does not go to zero below E_F, has a much wider range of finite values, but is reminiscent of the pseudogap (dip) by showing a double peak structure with a minimum around–0.9 eV. The change in the band structure when TMD goes from ML to multilayer form is in keeping with previous work (NbS_2,[38] WS_2,[39] (MoS_2, WS_2, NbS_2, and ReS_2),[40] (MoS_2,WS_2,WSe_2, and $MoSe_2$)[1]). These features of the NbS_2/WSe_2 VH may be advantageous in a possible use as a field effect transistor, because the much broader range of finite transmission would make it more stable, while the double-peak shape could be exploited to obtain fine effects.

Clearly, the previous arguments are based on the relative alignment of the work function of NbS_2 and the TVB of WSe_2. It is thus important to validate our predicted values for these quantities against experiment and previous work. For the work function of NbS_2 we predict a value of 6.08 eV for the ML system (see also ref. [20]) that is in good agreement with computational literature data,[41] while we obtain 6.15 eV for the 2H bulk which is also in good agreement with previously reported data.[18]

For the TVB of WSe_2 we obtain values of 5.038 eV for the ML system and 4.936 eV for the 2H bulk. These values are rather insensitive to the level of the DFT approach, and are basically coincident if one uses a gradient-corrected (GGA, semilocal) exchange-correlation (xc-) functional as we have done in the present work or uses a hybrid xc-functional.[41] The situation is less clear at the experimental level. Some experiments report values of the work function of NbS_2 much lower than 6 eV, around 4–5 eV (4 eV with an associated error of 1 eV in ref. [42], 4.9 eV in ref. [43]). However, these values were extracted from experiments conducted on highly defected NbS_2 samples, and it is to be expected that the work function of NbS_2 is very sensitive to defects, impurities, etc. More reliably, a NbS_2/MoS_2 system was investigated.[11] The authors created thick stripes of NbS_2 and MoS_2 intersecting orthogonally and measured the work function of both system via Kelvin Probe Microscopy. It is important to underline that, under the conditions of the experimental set-up, the systems are highly n-doped, so that the measured values of the work function of these systems corresponds to the TVB of NbS_2 and the BCB of MoS_2, i.e., the valence band of NbS_2 is filled under the conditions of the experiment. The experimentally measured values are 4.81 eV for the TVB of NbS_2 and 4.53 eV for the BCB of MoS_2. The value of 4.53 eV for the BCB of MoS_2 is in keeping with previous literature,[44,45] (doped with O_2). The TVB of NbS_2 is predicted to be 5.2 eV at the PBE GGA level and 4.8 eV by the hybrid HSE xc-functional. The agreement between the NbS_2 TVB value measured in experiment and that predicted by the hybrid xc-functional is thus excellent. It can be noted that, whereas the lower region of the NbS_2 valence band and therefore the value of the work function are rather insensitive to the DFT approach, the top of the band comes out to be wider at the hybrid level, thus the larger discrepancy in the TVB value using GGA xc-functionals. However, the good match between the work function of NbS_2 via hybrid and GGA xc-functionals validates the accuracy of our DFT approach for the NbS2/WSe2 system.

3.2.2. Other Stacking Epitaxies

We performed transmission simulations for all the five stacking geometries introduced in Section 2 (see Figure 1). Moreover, to investigate the effects of a misorientation of the NbS_2 with respect to the WSe_2 phase, as in ref. [25], we considered the three systems exhibiting hollow stacking, i.e., AA', AB', and AB, at two different values of the interfacial distance between S and Se atoms: a closest-approach distance between S and Se (normal distance), that we expect in the case of the energetically favorable epitaxy, and a "on-top" distance between S and Se atoms at the interface that corresponds to the interlayer spacing occurring for systems with on-top stacking, i.e., AA and A'B (top distance). The rationale for this choice is that a misorientation of the NbS_2 and WSe_2 fragments entails that in some region an on-top stacking will be realized, that will enforce an increase in the interlayer distance also for the hollow stackings in other regions of the VH.[25] We report the results of all these transmission simulations in **Figure 5**, illustrating the comparison between normal and on-top distances for the three systems with hollow stacking (Figure 5a–c), and separately the two systems with on-top stacking (Figure 5d). From Figure 5, we first observe that the transmission interval is similar for all stacking systems, so we predict that this feature will not be affected by a misorientation of the NbS_2 with respect to the WSe_2 phases. In contrast, the double-peak behavior is considerably lost when we increase the distances from normal to on-top for the three systems with hollow stacking. This phenomenon is most obvious for the AB stacking (Figure 5c). To understand this finding in more depth, we focus on the AB phase here, while an analysis of the other two stackings is provided in the Supporting Information, Section 4.3.

We focus on two bias values with distinct changes in the transmission coefficient between normal and on-top distances, as highlighted in Figure 5c: E = –0.95 eV, where a dip is found for normal distance, and –1.05 eV, where a maximum is found for normal distance. We then analyze the output of transmission simulations and single out the k-points which exhibit nonzero transmission at these two energies, thus dominating transmission. We then calculate and plot the PDOS of the interface atoms at these energies and at these *k*-points (the PDOS of the atoms far from the interface is not affected by the chosen interfacial distance, as shown in Figure S7, Supporting Information), and report the corresponding plots in **Figure 6**. First, in Figure 6 we note a shift in the PDOS of the interfacial atoms to higher energies when the distance changes from normal to top. This however cannot be the reason of the change in the peak versus dip in transmission because the changes in PDOS apparently do not correlate with the changes

 © 2022 The Authors. Advanced Electronic Materials published by Wiley-VCH GmbH

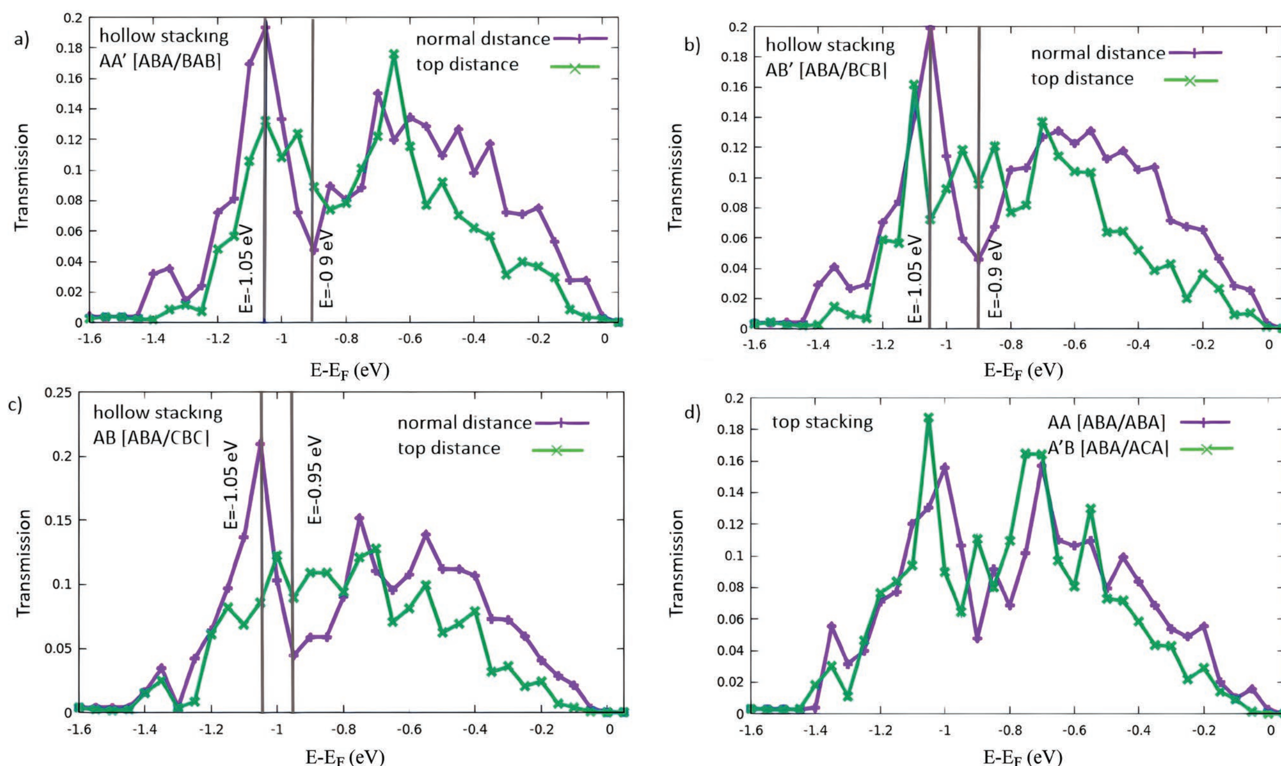

Figure 5. Transmission coefficient of all stacking systems: a) hollow stacking AA' with normal distance and top distance at the interface, b) hollow stacking AB' with normal distance and top distance at the interface, c) hollow stacking AB with normal distance and top distance at the interface and d) top stacking AA and A'B.

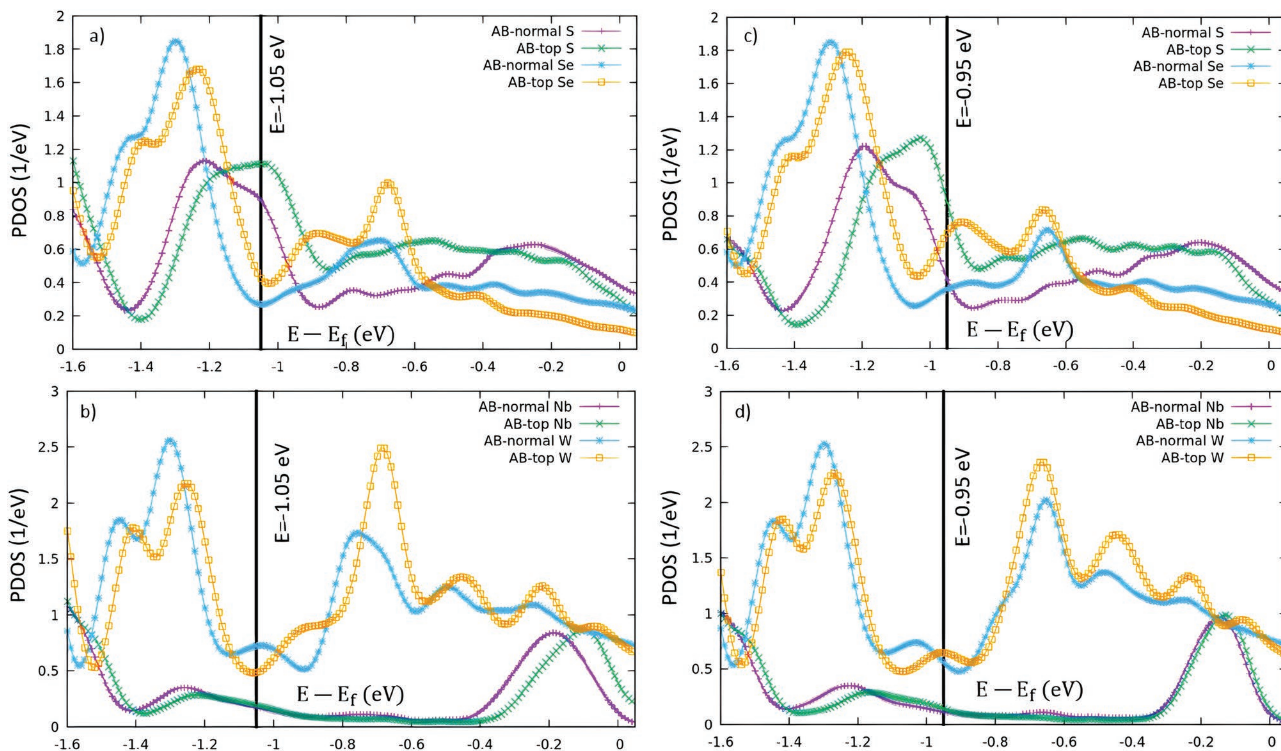

Figure 6. PDOS plots of atoms at the interfaces of AB structure for both normal and top distances: a) PDOS of chalcogen atoms for the *k*-points with ninzero tranmission in $E = -1.05$ eV, b) PDOS of metal atoms for the *k*-points with nonzero transmission in $E = -1.05$ eV, c) PDOS of chalcogen atoms for the *k*-points with ninzero tranmission in $E = -0.95$ eV, d) PDOS of metal atoms for the *k*-points with nonzero transmission in $E = -0.95$ eV.

© 2022 The Authors. Advanced Electronic Materials published by Wiley-VCH GmbH

in transmission. For example, at $E = -1.05$ eV, at which bias we calculate a higher transmission coefficient for normal distance, the PDOS of most of the atoms at the interface is actually lower at normal distance with respect to on-top distance (only the PDOS of W at the interface is slightly higher at normal distance). A different phenomenon must then be responsible for the observed transmission behavior. We then hypothesize that the lower transmission predicted for the top-distance systems is due to the fact that, when the distance increases, the atomic orbitals of the interfacial atoms become more localized and the corresponding orbital overlaps decreases. To prove this, we performed a Wannier analysis of the wave function, determining the hopping elements from the Wannier90 Hamiltonian matrix.[34,35] Then, we use a simple analytic formula and approximate transmission as the product of the PDOS and Wannier hopping matrix elements between the atoms at the interface. We estimate the current as[46]

$$I = \frac{2e}{h}\int dE\, T(E)\left[f_L(E) - f_R(E)\right] \tag{1}$$

where $T(E)$ is the transmission coefficient and $f_\alpha(E)$ is the Fermi-Dirac distribution function for lead $\alpha = L$ or R. In a simplified model with discrete energy levels, when we are in linear response regime, Equation (1) can be written as[47]

$$I = \frac{e}{\hbar}\int_{-\infty}^{+\infty} dE\, D(E)\frac{(\gamma_1\gamma_2)}{\gamma_1+\gamma_2}\left[f_1(E) - f_2(E)\right] \tag{2}$$

where $D(E)$ is the DOS at the energy E, and γ_1 (γ_2) is the coupling strength (hopping). Clearly, this approximation is quantitatively accurate only at low temperatures and modest values of the bias.[47]

From Equations (1) and (2), we get approximately

$$T(E) \approx D(E)\frac{(\gamma_1\gamma_2)}{\gamma_1+\gamma_2} \tag{3}$$

To apply Equation (3) to our systems, we choose two paths for electron transmission, each consisting of two jumps (see Figure S8 in the Supporting Information)

Path A: Nb → Se // Se → W

Path B: Nb → S // S → W

where the T(E) corresponding to each jump can be estimated as a product of the DOS on the involved Nb/W/S/Se atomic orbitals times the corresponding Wannier matrix elements among atomic orbitals, i.e.

$$\mathrm{T(E)\,(path\ A\ via\ Se\ atom)} \approx \mathrm{PDOS(Nb)\,PDOS(Se)\,PDOS(W)\,H(Nb,Se)\,H(W,Se)} \tag{4a}$$

$$\mathrm{T(E)\,(path\ B\ via\ S\ atom)} \approx \mathrm{PDOS(Nb)\,PDOS(S)\,PDOS(W)\,H(Nb,S)\,H(W,S)} \tag{4b}$$

where H(a,b) is the matrix element of the Wannier90 Hamiltonian corresponding to the hopping between the orbitals of atoms a and b, PDOS(c) is the PDOS of an orbital corresponding to the given atom c, and to make the notation simpler we have not indicated explicitly the atomic orbitals, but a sum over all atomic orbital is implied in Equations (4a,b). In **Tables 1** and **2**, we report the approximate values of transmission obtained using this simple formula at $E = -1.05$ eV and $E = -0.95$ eV, respectively. Notably, we find an excellent agreement between the transmission values estimated via the approximate formula and the full transmission results of Figure 5c: the transmission values via the dominating path B in the approximate formula closely correspond in ratio to those of the exact calculations.

Table 1. Values of transmission along path A (via Se) and path B (via S) using the approximate formulae Equation (4) at a bias $E = -1.05$ eV.

$E = -1.05$ eV	Transmission
Normal	0.0585 (via Se) – 0.275 (via S)
Top	0.0534 (via Se) – 0.1654 (via S)

It is worth noting in passing that the value of transmission in path B (via S) is higher than in path A (via Se) because of two reasons: first, the higher PDOS of S with respect to Se at the interface; second, the bigger hopping matrix element between W and S [H (W, S)] with respect to the hopping between Nb and Se [H (Nb, Se)]. Tables S2 and S3 in the Supporting Information, Section 4.2, report full details of these calculations.

4. Conclusions

In summary, we have investigated a metal (NbS_2)/semiconductor (WSe_2) VH via DFT and transmission simulations. We consider individual fragments in the VH to be in 2H bulk phases and we change the geometry at the interface according to all 5 possible epitaxial stackings. We perform band structure QM simulations ensuring convergence of periodic models and investigate the transport properties of the VHs. We find that the transmission profile as a function of bias exhibits a wide finite interval and a double-peak structure for all 5 stackings when at contact distance. We then analyze the electrostatic potential profile and estimate the transmission behavior either using band alignment of the separated fragments, or using PDOS in the scattering region, obtaining results consistent between the two approaches and in agreement, and therefore fully rationalizing, the exact simulations. In contrast, the transmission profile flattens when the distance between the chalcogen atoms at the interfaces increases from contact (normal) to on-top distances (simulating of misorientation of the layers at the interface). Importantly, in this case band alignment arguments are not sufficient to explain this behavior. We thus introduce a simple transmission model that includes Wannier transfer matrix elements at the interface. This extended model now allows us to rationalize quantitatively our findings. Interestingly, the interval of nonzero transmission coefficient for the NbS_2/WSe_2 VH is qualitatively similar but much wider with respect to the previously investigated LH.[20]

Table 2. Values of transmission along path A (via Se) and path B (via S) using the approximate formulae Equation (4) at a bias $E = -0.95$ eV.

$E = -0.95$ eV	Transmission
Normal	0.0395 (via Se) – 0.0645 (via S)
Top	0.0859 (via Se) – 0.1285 (via S)

 © 2022 The Authors. Advanced Electronic Materials published by Wiley-VCH GmbH

This, together with two-peak structure in transmission, makes this system potentially interesting for applications in electronic devices.

Supporting Information

Supporting Information is available from the Wiley Online Library or from the author.

Acknowledgements

The ISCRA programme of the CINECA supercomputing Center (LHFET-BS project) is gratefully acknowledged for computational resources. This project has received funding from the European Union's Horizon 2020 research and innovation programme under Grant Agreement No. 829 035 (QUEFORMAL, https://www.queformal.eu/), and from the MIUR PRIN Five2D project under Grant Agreement No. 2017SRYEJH.

Open access funding provided by Consiglio Nazionale delle Ricerche within the CRUI-CARE Agreement.

Conflict of Interest

The authors declare no conflict of interest.

Data Availability Statement

The data that support the findings of this study are available in the Supporting Information of this article.

Keywords

background electrostatic potential, band alignment, electron transport analysis, fragment decomposition, quantum mechanical modeling, vertical heterostructures, 2D materials

Received: January 5, 2022
Revised: February 18, 2022
Published online: April 17, 2022

[1] X. Zhang, X. F. Qiao, W. Shi, J. B. Wu, D. S. Jiang, P. H. Tan, *Chem. Soc. Rev.* **2015**, *44*, 2757.
[2] N. Peimyoo, W. Yang, J. Shang, X. Shen, Y. Wang, T. Yu, *ACS Nano* **2014**, *8*, 11320.
[3] Y. Liu, J. Guo, E. Zhu, L. Liao, S. J. Lee, M. Ding, I. Shakir, V. Gambin, Y. Huang, X. Duan, *Nature* **2018**, *557*, 696.
[4] C. M. Went, J. Wong, P. R. Jahelka, M. Kelzenberg, S. Biswas, M. S. Hunt, A. Carbone, H. A. Atwater, *Sci. Adv.* **2019**, *5*, eaax6061.
[5] V. Agafonov, V. Nargelienė, S. Balakauskas, V. Bukauskas, M. Kamarauskas, A. Lukša, A. Mironas, A. Rėza, A. Šetkus, *Nanotechnology* **2019**, *31*, 025602.
[6] G. Iannaccone, F. Bonaccorso, L. Colombo, G. Fiori, *Nat. Nanotechnol.* **2018**, *13*, 183.
[7] E. G. Marin, D. Marian, M. Perucchini, G. Fiori, G. Iannaccone, *ACS Nano* **2020**, *14*, 1982.
[8] H. Hu, Z. Zhang, G. Ouyang, *Appl. Surf. Sci.* **2020**, *517*, 146168.
[9] C. Gong, L. Colombo, R. M. Wallace, K. Cho, *Nano Lett.* **2014**, *14*, 1714.
[10] C. Zhang, C. Gong, Y. Nie, K. A. Min, C. Liang, Y. J. Oh, H. Zhang, W. Wang, S. Hong, L. Colombo, R. M. Wallace, *2D Mater.* **2016**, *4*, 015026.
[11] H. G. Shin, H. S. Yoon, J. S. Kim, M. Kim, J. Y. Lim, S. Yu, J. H. Park, Y. Yi, T. Kim, S. C. Jun, S. Im, *Nano Lett.* **2018**, *18*, 1937.
[12] H. Fang, C. Battaglia, C. Carraro, S. Nemsak, B. Ozdol, J. S. Kang, H. A. Bechtel, S. B. Desai, F. Kronast, A. A. Unal, G. Conti, *Proc. Natl. Acad. Sci. USA* **2014**, *111*, 6198.
[13] X. Hong, J. Kim, S. F. Shi, Y. Zhang, C. Jin, Y. Sun, S. Tongay, J. Wu, Y. Zhang, F. Wang, *Nat. Nanotechnol.* **2014**, *9*, 682.
[14] N. Huo, S. Tongay, W. Guo, R. Li, C. Fan, F. Lu, J. Yang, B. Li, Y. Li, Z. Wei, *Adv. Electron. Mater.* **2015**, *1*, 1400066.
[15] N. Huo, J. Kang, Z. Wei, S. S. Li, J. Li, S. H. Wei, *Adv. Funct. Mater.* **2014**, *24*, 7025.
[16] C. H. Lee, G. H. Lee, A. M. V. D. Zande, W. Chen, Y. Li, M. Han, X. Cui, G. Arefe, C. Nuckolls, T. F. Heinz, J. Guo, *Nat. Nanotechnol.* **2014**, *9*, 676.
[17] J. Y. Lim, M. Kim, Y. Jeong, K. R. Ko, S. Yu, H. G. Shin, J. Y. Moon, Y. J. Choi, Y. Yi, T. Kim, S. Im, *NPJ 2D Mater. Appl.* **2018**, *2*, 19.
[18] A. L. M. T. Costa, F. W. N. Silva, E. B. Barros, *Semicond. Sci. Technol.* **2018**, *33*, 075018.
[19] L. Jelver, D. Stradi, K. Stokbro, K. W. Jacobsen, *Nanoscale Adv.* **2021**, *3*, 567.
[20] Z. Golsanamlou, L. Sementa, T. Cusati, G. Iannaccone, A. Fortunelli, *Adv. Theory Simul.* **2021**, *4*, 2100164.
[21] T. Cusati, G. Fiori, A. Gahoi, V. Passi, M. C. Lemme, A. Fortunelli, G. Iannaccone, *Sci. Rep.* **2017**, *7*, 5109.
[22] D. Szczęśniak, R. D. Hoehn, S. Kais, *Phys. Rev. B* **2018**, *97*, 195315.
[23] Y. Guo, D. Liu, J. Robertson, *ACS Appl. Mater. Interfaces* **2015**, *7*, 25709.
[24] K. Ren, M. Sun, Y. Luo, S. Wang, Y. Xu, J. Yu, W. Tang, *Phys. Lett. A* **2019**, *383*, 1487.
[25] T. Cusati, A. Fortunelli, G. Fiori, G. Iannaccone, *Phys. Rev. B* **2018**, *98*, 115403.
[26] X. Ding, S. Zhang, M. Zhao, Y. Xiang, K. H. Zhang, X. Zu, S. Li, L. Qiao, *Phys. Rev. Appl.* **2019**, *12*, 064061.
[27] X. Ding, Y. Zhao, H. Xiao, L. Qiao, *Appl. Phys. Lett.* **2021**, *118*, 091601.
[28] D. B. de Araújo, R. Q. Almeida, A. C. Gadelha, N. P. Rezende, F. C. C. S. Salomão, F. W. N. Silva, L. C. Campos, E. B. Barros, *2D Mater.* **2020**, *7*, 045029.
[29] P. Giannozzi, S. Baroni, N. Bonini, M. Calandra, R. Car, C. Cavazzoni, D. Ceresoli, G. L. Chiarotti, M. Cococcioni, I. Dabo, A. D. Corso, S. de Gironcoli, S. Fabris, G. Fratesi, R. Gebauer, U. Gerstmann, C. Gougoussis, A. Kokalj, M. Lazzeri, L. Martin-Samos, N. Marzari, F. Mauri, R. Mazzarello, S. Paolini, A. Pasquarello, L. Paulatto, C. Sbraccia, S. Scandolo, et al., *J. Phys.: Condens. Matter* **2009**, *21*, 395502.
[30] P. Giannozzi, O. Andreussi, T. Brumme, O. Bunau, M. B. Nardelli, M. Calandra, R. Car, C. Cavazzoni, D. Ceresoli, M. Cococcioni, N. Colonna, I. Carnimeo, A. Dal Corso, S. de Gironcoli, P. Delugas, R. A. DiStasio, A. Ferretti, A. Floris, G. Fratesi, G. Fugallo, R. Gebauer, U. Gerstmann, F. Giustino, T. Gorni, J. Jia, M. Kawamura, H.-Y. Ko, A. Kokalj, E. Küçükbenli, M. Lazzeri, et al., *J. Phys.: Condens. Matter* **2017**, *29*, 465901.
[31] J. P. Perdew, K. Burke, M. Ernzerhof, *Phys. Rev. Lett.* **1996**, *77*, 3865.
[32] A. Smogunov, A. D. Corso, E. Tosatti, *Phys. Rev. B* **2004**, *70*, 045417.
[33] H. J. Choi, J. Ihm, *Phys. Rev. B* **1999**, *59*, 2267.
[34] N. Marzari, D. Vanderbilt, *Phys. Rev. B* **1997**, *56*, 12847.
[35] A. A. Mostofi, J. R. Yates, Y. S. Lee, I. Souza, D. Vanderbilt, N. Marzari, *Comput. Phys. Commun.* **2008**, *178*, 685.
[36] M. Leroux, M. Le Tacon, M. Calandra, L. Cario, M-A. Méasson, P. Diener, E. Borrissenko, A. Bosak, P. Rodière, *Phys. Rev. B* **2012**, *86*, 155125.
[37] J. He, K. Hummer, C. Franchini, *Phys. Rev. B* **2014**, *89*, 075409.

© 2022 The Authors. Advanced Electronic Materials published by Wiley-VCH GmbH

[38] C. Heil, M. Schlipf, F. Giustino, *Phys. Rev. B* **2018**, *98*, 075120.
[39] J. He, D. He, Y. Wang, Q. Cui, F. Ceballos, H. Zhao, *Nanoscale* **2015**, *7*, 9526.
[40] A. Kuc, N. Zibouche, T. Heine, *Phys. Rev. B* **2011**, *83*, 245213.
[41] https://cmrdb.fysik.dtu.dk/c2db/ (accessed: February 2022).
[42] C. Battaglia, H. Cercellier, L. Despont, C. Monney, M. Prester, H. Berger, L. Forr'o, M. G. Garnier, P. Aebi, *Eur. Phys. J. B* **2007**, *57*, 385.
[43] Y. Choi, H. Bark, B. Kang, M. Lee, B. Kim, S. Lee, C. Lee, J. H. Cho, *J. Mater. Chem. C* **2019**, *7*, 8599.
[44] O. Ochedowski, K. Marinov, N. Scheuschner, A. Poloczek, B. K. Bussmann, J. Maultzsch, M. Schleberger, *Beilstein J. Nanotechnol.* **2014**, *5*, 291.
[45] S. Y. Lee, U. J. Kim, J. Chung, H. Nam, H. Y. Jeong, G. H. Han, H. Kim, H. M. Oh, H. Lee, H. Kim, Y. G. Roh, J. Kim, S. W. Hwang, Y. Park, Y. H. Lee, *ACS Nano* **2016**, *10*, 6100.
[46] Y. Meir, N. S. Wingreen, *Phys. Rev. Lett.* **1992**, *68*, 2512.
[47] S. Datta, *Quantum Transport: Atom to Transistor*, Cambridge University Press, Cambridge **2005**.

© 2022 The Authors. Advanced Electronic Materials published by Wiley-VCH GmbH